The Astrophysical Journal, 770:6 (12pp), 2013 June 10 doi:10.1088/0004-637X/770/1/6


# INJECTION OF PLASMA INTO THE NASCENT SOLAR WIND VIA RECONNECTION DRIVEN BY SUPERGRANULAR ADVECTION

Liping Yang[1,2], Jiansen He[1], Hardi Peter[3], Chuanyi Tu[1], Wenlei Chen[1], Lei Zhang[1], Eckart Marsch[4], Linghua Wang[1], Xueshang Feng[2], and Limei Yan[1]
[1] School of Earth and Space Sciences, Peking University, 100871 Beijing, China; jshept@gmail.com
[2] SIGMA Weather Group, State Key Laboratory for Space Weather, Center for Space Science and Applied Research, Chinese Academy of Sciences, 100871 Beijing, China
[3] Max-Planck-Institut für Sonnensystemforschung, Max-Planck-Strasse, D-37191 Katlenburg-Lindau, Germany
[4] Institute for Experimental and Applied Physics, Christian Albrechts University at Kiel, D-24118 Kiel, Germany
*Received 2012 August 16; accepted 2013 March 18; published 2013 May 17*

## ABSTRACT

To understand the origin of the solar wind is one of the key research topics in modern solar and heliospheric physics. Previous solar wind models assumed that plasma flows outward along a steady magnetic flux tube that reaches continuously from the photosphere through the chromosphere into the corona. Inspired by more recent comprehensive observations, Tu et al. suggested a new scenario for the origin of the solar wind, in which it flows out in a magnetically open coronal funnel and mass is provided to the funnel by small-scale side loops. Thus mass is supplied by means of magnetic reconnection that is driven by supergranular convection. To validate this scenario and simulate the processes involved, a 2.5 dimensional (2.5D) numerical MHD model is established in the present paper. In our simulation a closed loop moves toward an open funnel, which has opposite polarity and is located at the edge of a supergranulation cell, and magnetic reconnection is triggered and continues while gradually opening up one half of the closed loop. Its other half connects with the root of the open funnel and forms a new closed loop which is submerged by a reconnection plasma stream flowing downward. Thus we find that the outflowing plasma in the newly reconnected funnel originates not only from the upward reconnection flow but also from the high-pressure leg of the originally closed loop. This implies an efficient supply of mass from the dense loop to the dilute funnel. The mass flux of the outflow released from the funnel considered in our study is calculated to be appropriate for providing the mass flux at the coronal base of the solar wind, though additional heating and acceleration mechanisms are necessary to keep the velocity at the higher location. Our numerical model demonstrates that in the funnel the mass for the solar wind may be supplied from adjacent closed loops via magnetic reconnection as well as directly from the footpoints of open funnels.

*Key words:* magnetic reconnection – solar wind – Sun: chromosphere – Sun: corona

*Online-only material:* color figures

## 1. INTRODUCTION

The solar wind is a continuous stream of high-temperature plasma that flows away from the Sun. The existence of the solar wind was first proposed by Biermann (1951), who observed the phenomenon that the tail of a comet always points away from the Sun. Parker (1958) established a solar wind fluid model based on an isothermal expansion of the corona. From his single-fluid equations he obtained a critical solution for which the flow became supersonic, which he called the "solar wind." In 1959 January, for the first time the Soviet spacecraft *Luna 1* directly detected the solar wind and verified Parker's prediction (Beatty 2007). From then on, the solar wind has been investigated intensively by in situ measurements, remote-sensing observations and theoretical studies. Thus by more than half a century of spacecraft exploration and theoretical research, we have acquired detailed knowledge about the characteristics of the solar wind in interplanetary space (Marsch 2006). More recently, a deeper understanding of the conditions prevailing in the solar wind source region was also achieved, e.g., concerning element abundances, flow fields, magnetic structure, temporal intermittency, etc. (Hassler et al. 1999; Peter & Judge 1999; Xia et al. 2004; Feldman et al. 2005; Tu et al. 2005a, 2005b; He et al. 2007, 2010a, 2010b, 2010c; Tian et al. 2008, 2010). However, how exactly the solar wind plasma is generated and replenished in the solar atmosphere still remains a mystery.

In many previous models of the solar wind the authors concentrated on its heating and acceleration in a given one-dimensional magnetic flux tube or plasma flow tube (Parker 1958; Whang & Chang 1965; Leer & Holzer 1980; Hollweg 1986; Tu 1988; Wang & Sheeley 1991; Hansteen & Leer 1995; Tu & Marsch 1997; Marsch & Tu 1997; Hollweg & Isenberg 2002; Suzuki & Inutsuka 2005; Cranmer et al. 2007; Verdini et al. 2010; Matsumoto & Suzuki 2012). These models improved Parker's original model in three main aspects. First, the location where the solar wind starts to flow outward was redefined and moved from the coronal base (Parker 1958; Whang & Chang 1965; Leer & Holzer 1980) to the lower solar atmosphere (Hollweg 1986; Hansteen & Leer 1995; Tu & Marsch 1997; Suzuki & Inutsuka 2005; Cranmer et al. 2007). This implied that coronal heating and solar wind acceleration should not be seen as separate processes but be treated together and described by the same model. Another major improvement was the inclusion of (the chromosphere and) the transition region at the base of the corona in the solar wind models (Hammer 1982a, 1982b). This also required a proper treatment of the heat conduction back toward the Sun (Withbroe 1988), with the consequence that the solar wind mass loss rate would basically be determined by the energy input into the combined chromosphere–corona–solar wind system (Hansteen & Leer 1995). Second, the geometry of the flow tube was described by a height-dependent profile of its cross-section (Kopp & Holzer 1976; Marsch & Tu 1997;

Hackenberg et al. 2000; Tu et al. 2005a). In the corona, the cross-sections were often configured such that their shapes imitated the coronal hole boundaries. For the region from the chromosphere to corona, the shape was considered to be funnel-like. Third, the heating and acceleration of the solar wind was achieved by employing various mechanisms of energy conversion (Hansteen & Leer 1995; Tu & Marsch 1997; Suzuki & Inutsuka 2005; Cranmer et al. 2007; Verdini et al. 2010). Furthermore, multi-dimensional solar wind models were constructed. Instead of properly including the chromosphere, most of them, while considering coronal heating (e.g., Chen & Hu 2001; Riley et al. 2001; Li et al. 2004; van der Holst et al. 2010; Yang et al. 2011; Feng et al. 2011, 2012), assumed the coronal base as the lower boundary.

Previous 1D solar wind models could not explain the transition of Doppler shifts from red to blue as observed from the chromosphere to the corona (Peter & Judge 1999; Tu et al. 2005b). Correlating the radiance and Doppler-shift maps with the extrapolated magnetic structures throughout the transition region in the polar coronal hole, Tu et al. (2005b) found that the correlation heights (formation heights) of the Si II, C IV, and Ne VIII lines are approximately 4, 5, and 24 Mm. The area-averaged Doppler shifts for these lines are −2, 0, and +10 km $s^{-1}$, respectively, with positive (negative) sign representing upflow (downflow). Thus when going upward in the atmosphere from the chromosphere via the transition region to the corona, the observed Doppler shift turns from red to zero to blue.

On this observational basis, Tu et al. (2005a, 2005b) suggested a new scenario of the solar wind origin in a coronal hole. Driven by supergranular convection in the photosphere, the meso-scale closed loops with heights of less than 5 Mm existing in the interior of a supergranule will be advected toward the edges along with the supergranular flow. Finally, the horizontally moving loops will impinge on an open funnel located at the supergranular cell boundary, and this collision may trigger reconnection between them. Thereby, the plasma previously confined in the loop can be released, a process which generates plasma parcels flowing both upward and downward. The upflowing plasma may be further heated and accelerated, e.g., by wave dissipation, and thus form the nascent solar wind. In this model, the horizontal exchange of mass and energy between neighboring flux tubes occurs in the lower transition region below about ∼5 Mm. After the reconnection between the open network field and side magnetic loops has gradually ceased, the vertical will become more important than the horizontal motion, and thus the radial acceleration of the solar wind will actually start. A detailed illustration of this scenario will be presented in Section 2.1, as the physical concept underlying our simulation.

Following this scenario suggested by Tu et al. (2005a, 2005b), He et al. (2008) put forward a 1D fluid model to explain the solar wind origin. In that model, it was assumed that mass and energy are deposited in the open funnel at 5 Mm. The mass supply rate was estimated from the mass loss rate as given by the emptying of the neighboring loops, and the energy input rate was defined to be consistent with the release rate as determined by reconnection between the open funnel and closed loops. This model did produce plasma flowing not only upward to form the solar wind but also downward back to the lower atmosphere, a result which supports the scenario of solar wind origin as proposed by Tu et al. (2005a, 2005b). However, this model needs to be extended to higher dimensions, in order to take self-consistently into account the possible magnetic reconnection between open funnels and closed loops.

So far, the dynamic plasma processes associated with magnetic reconnection in the solar atmosphere have been intensively investigated by means of MHD simulations (Yokoyama & Shibata 1994, 1995, 1996; Shimojo et al. 2001; Miyagoshi & Yokoyama 2004; Nishizuka et al. 2008; Gudiksen & Nordlund 2002, 2005; Peter et al. 2004, 2006; Bingert & Peter 2011; Büchner et al. 2004; Büchner & Nikutowski 2005; Santos & Büchner 2007; Zhang & Wu 2009). To examine the magnetic reconfiguration occurring in X-ray jets, Yokoyama & Shibata (1995, 1996) performed MHD simulations and thus explored the reconnection between the emerging flux and the nearly uniform coronal fields, which was driven the magnetic buoyancy instability. With a more realistic temperature and density distribution in the corona, Nishizuka et al. (2008) extended this model to simulate a giant jet with both cool and hot components as discovered by *Hinode*. To investigate the direct current dissipation mechanism for coronal heating (Parker 1972; van Ballegooijen 1986), Gudiksen & Nordlund (2002, 2005) presented a 3D MHD model, which includes the atmospheric layers from the photosphere to the lower corona, and realistically accounts for the mass, momentum, and energy balance. Driven by the supergranular motion in the photosphere, this model produced heating of the corona in just the way Parker (1972) suggested. Büchner & Nikutowski (2005) also conducted a numerical experiment to study the reconnection between low-lying loops and funnel-shaped magnetic fields, which was driven by photosphere vortex motion. They found that the resulting reconnection could accelerate the heated plasma to certain initial velocities. However, in their simulation they used a simplified energy equation, which did not account for heat conduction or energy losses through optically thin radiation.

According to solar observations, coronal bright points (CBPs) are ubiquitous in coronal hole and quiet Sun regions (e.g., Kamio et al. 2007; Dere 2008; Tian et al. 2008). These CBPs usually resemble loop-like structures, with a typical temperature of $10^6$ K and a density of $10^9$ $cm^{-3}$ near the apex (Doschek et al. 2010). CBPs are sometimes observed to be associated with coronal jets, revealing magnetic reconnection between the hot closed loop and ambient open field lines (e.g., Cirtain et al. 2007; He et al. 2010a). The magnetic field strength at the foot of a CBP is usually tens of Gauss (He et al. 2010a).

In this paper, we will simulate the reconnection between a closed loop and an open funnel. The closed loop in our simulation has a size comparable with that of observed CBPs, which is much smaller than that of a large trans-network closed loop being associated with the observed plume-like coronal structures. Moreover, the closed loop has a temperature, density, and magnetic strength similar to that of the observed CBPs. Our aim is to examine the consequences of the model for the solar wind origin suggested by Tu et al. (2005a, 2005b), and to provide results supporting this scenario. For this purpose, a 2.5D MHD simulation model is developed with a domain reaching from the upper chromosphere to the lower corona, and a realistic energy equation is considered, which among others includes in particular heat conduction, radiation losses, and loop heating. With this MHD model, we can realistically simulate reconnection occurring between the open funnel fields and low-lying loops. The latter are advected by the supergranular convection flow toward the network boundary.

The paper is organized as follows. In Section 2, a general description of the numerical MHD model is given, which

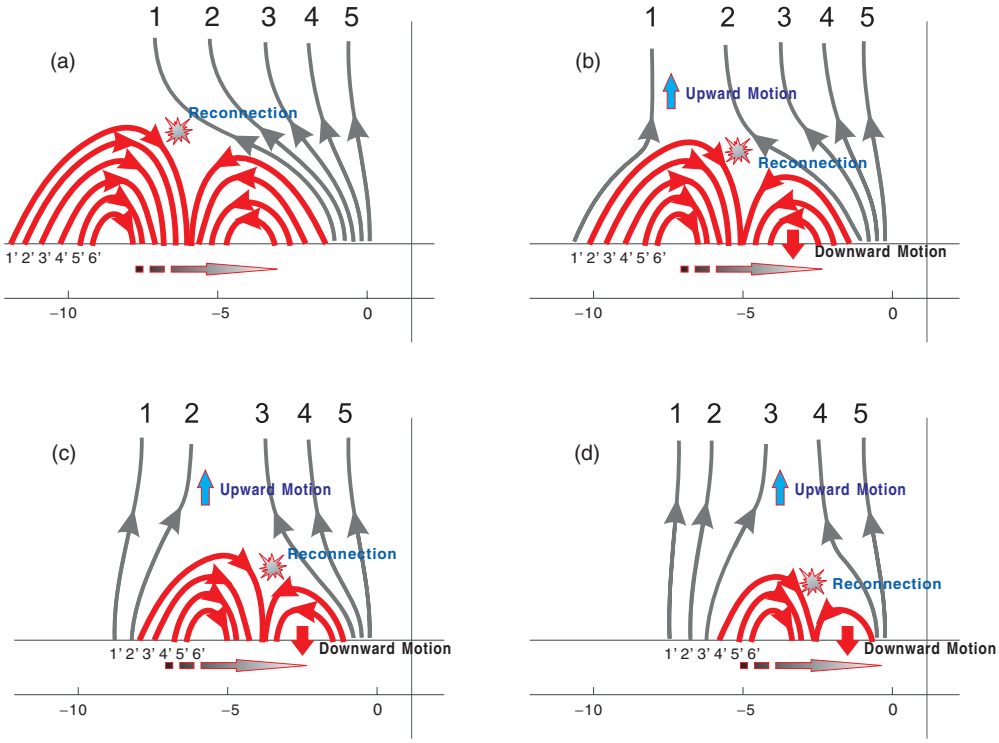


**Figure 1.** Sketch to illustrate the scenario of the solar wind origin.
(A color version of this figure is available in the online journal.)

includes the physical concept of solar wind origin. Section 3 describes the results of the numerical simulation and their analysis. Section 4 is reserved for the summary and discussion.

## 2. NUMERICAL MHD MODEL

### 2.1. The Concept of the Solar Wind Origin in 2D Scenario

The basic picture of how the solar wind originates, as suggested by Tu et al. (2005a, 2005b), is illustrated as a sketch in Figure 1, where an open funnel (right) and a hot dense loop (left) are shown. Being transported by the horizontal supergranular flow, a hot dense loop migrates toward the edges of an open funnel that has a magnetic field of opposite polarity. Consequently, a current sheet is formed at the interface between loop and funnel. Due to finite resistivity, the hot dense loop can reconnect with the open magnetic funnel. This process generates a small secondary loop, which bridges the endpoints of the original loop and the funnel, as well as a new field line that opens into the heliosphere. Simultaneously, two plasma streams are produced around the reconnection site. Accelerated by the tension force of these new field lines, one stream subducts the small loop into the photosphere (red arrow in panel (b)), while the other stream flows upward along the new open field line and contributes to the nascent solar wind (blue arrow in panel (b)). At the same time, magnetic energy is partly converted into thermal energy heating up the outflowing plasma. Driven by the horizontal flow, the hot dense loop continues to move toward the funnel and reconnects with the open field, until it totally disappears and the mass it contained is fully released. At the same time, the newly open field lines rearrange themselves, become located at the supergranulation boundary, and form funnel-shaped fields. When a new closed loop moves toward the network boundary, this process takes place once more, and another upstream is generated. Through this process, i.e., ultimately by the continuous advection of small loops toward the network boundaries, mass is intermittently supplied to the nascent solar wind.

### 2.2. Basic Equations and Numerical Method

We solve the 2.5D resistive MHD equations in Cartesian coordinates $(x, y, z)$, with $y$ directed vertically. We write these equations in the following non-dimensional form:

$$\frac{\partial \rho}{\partial t} + \nabla \cdot \rho \mathbf{u} = 0, \tag{1}$$

$$\frac{\partial \rho \mathbf{u}}{\partial t} + \nabla \cdot \left[ \rho \mathbf{u}\mathbf{u} + \mathbf{I}\left(p + \frac{1}{2}\mathbf{B}^2\right) - \mathbf{B}\mathbf{B} \right] = \rho \mathbf{g}, \tag{2}$$

$$\frac{\partial e}{\partial t} + \nabla \cdot \left[ \mathbf{u}\left(e + p + \frac{1}{2}\mathbf{B}^2\right) - (\mathbf{u}\cdot\mathbf{B})\mathbf{B} \right] = \rho \mathbf{u}\cdot\mathbf{g} + \nabla\cdot(\mathbf{B}\times\eta\mathbf{j}) - L_r + \nabla\cdot\mathbf{q} + H + C_N, \tag{3}$$

$$\frac{\partial \mathbf{B}}{\partial t} + \nabla \cdot (\mathbf{u}\mathbf{B} - \mathbf{B}\mathbf{u}) = \eta \nabla^2 \mathbf{B}, \tag{4}$$

where

$$e = \frac{1}{2}\rho \mathbf{u}^2 + \frac{p}{\gamma - 1} + \frac{1}{2}\mathbf{B}^2, \quad \mathbf{j} = \nabla \times \mathbf{B}, \tag{5}$$

which correspond to the total energy density and current density, respectively. Here, $\rho$ is the mass density; $\mathbf{u} = (v_x, v_y, v_z)$ are the velocities in the $x$, $y$, and $z$ directions; $p$ is the thermal pressure; $\mathbf{B}$ denotes the magnetic field; $t$ is time; $\mathbf{g}\ (= -g\mathbf{e}_y, g = \text{const})$ is the solar gravitational acceleration; and $\gamma = 5/3$ is the adiabatic index.

The magnetic resistivity $\eta$ is the current-dependent anomalous resistivity (Yokoyama & Shibata 1995, 1996; Büchner & Nikutowski 2005), which reads

$$\eta = \begin{cases} 0, & u_d \leqslant u_c \\ \alpha(u_d/u_c - 1)^2, & u_d > u_c \end{cases} \quad (6)$$

where $\alpha$ is the resistivity parameter and $u_d = J/\rho$ is the current-carrier velocity. $J$ is the total current density and $u_c$ is the threshold above which the anomalous resistivity is switched on. In this paper, $\alpha$ and $u_c$ are 0.01 and 100, respectively, and the typical magnetic Reynolds number (Rm) is obtained as $10^3$ at the location of reconnection with the following reasons. It is well known the current-driven micro-instabilities, such as ion acoustic instability, will trigger large enough local diffusion, which thereby reduce the local Rm value to be many orders of magnitude (i.e., $10^{-7}$) smaller than that due to Coulomb collisions (Treumann 2001; Büchner & Elkina 2005). Also, the value $10^3$ is suitable for our present computer resource in terms of computational time. When we test the simulation result with large Rm, such as $10^5$, we find similar mass release after reconnection although the reconnection becomes bursty as a result of the tearing instability.

In the energy equation, $L_r = N^2\Lambda(T)$ is the radiation loss and $\Lambda(T)$ is the radiative loss function, which is assumed to have the form given by Cook et al. (1989) for an optically thin medium. $\nabla \cdot \mathbf{q}$ relates to anisotropic thermal conduction, which plays an important role in the energy balance of the corona. The heat flux vector parallel to the magnetic field is

$$\mathbf{q} = K_\parallel(\hat{b} \cdot \nabla T)\hat{b}, \quad (7)$$

where $T$ is the temperature and $\hat{b}$ the unit vector of the magnetic field. Following Abbett (2007), the temperature-dependent coefficient of thermal conductivity is defined to be $K_\parallel = k_0 T^{5/2}$ when $T > T_c$ ($T_c \equiv 3 \times 10^5$ K) and $K_\parallel = k_0 T_c^{5/2}$ elsewhere ($k_0 = 1 \times 10^6$ in cgs units). To guarantee that the temperature near the bottom follows a profile similar to that in the model of Vernazza et al. (1981), we apply a Newton cooling term $C_N$ to the lowermost part of the model—the temperature in the chromosphere and corona remains unaffected by this. Like Bingert & Peter (2011) we use the following form:

$$C_N = \frac{\rho c_V}{\tau_{\rm cool}}(T_0 - T), \quad (8)$$

where $T_0$ is the initial temperature, and the cooling time scale $\tau_{\rm cool}$ is given by $\tau_{\rm cool} = \tau_0 \exp(y/h)$. We choose $\tau_0 = 2 \times 10^{-5}$ s and $h = 100$ km to make sure that $C_N$ has little impact on the temperature above 1 Mm. Finally, we specify a parameterized heating function $H$, which is composed of two terms,

$$H = H_{\rm exp} + H_{\rm loop}. \quad (9)$$

The first heating term $H_{\rm exp}$ is to maintain a background corona against conductive, radiative, and solar wind losses. Following Aiouaz et al. (2005), we allow it to vary with height $y$ as

$$H_{\rm exp} = \begin{cases} \dfrac{F}{\lambda}, & y \leqslant y_{\rm chr}, \\ \dfrac{F}{\lambda}\exp(-(y - y_{\rm chr})/\lambda), & y > y_{\rm chr}, \end{cases} \quad (10)$$

where the energy flux $F$ is 300 W m$^{-2}$, the damping length scale $\lambda$ is 5 Mm, and $y_{\rm chr}$ is set arbitrarily to 3 Mm. This form of the heating function has also often been used in 1D solar wind simulations (e.g., Hansteen & Leer 1995).

The second heating term $H_{\rm loop}$ is designed to maintain hot loops near the transition region. Due to the unknown loop heating mechanism and the lack of any other suitable expression, in the same way as Forbes & Malherbe (1991) we simply assume

$$H_{\rm loop} = C \times f_1 \times \rho, \quad (11)$$

where $C$ is a constant of about 1000 W m$^{-2}$, and $f_1$ has two values 1 and 0. $f_1$ is set to be 1 for the left loop region as sketched in Figure 1, and to be 0 elsewhere. In following section, we will elaborate how to select the time-varied left loop region for loop-heating in numerical calculation.

To normalize the MHD equations, we need three independent parameters: the reference density $\rho_0 = 2 \times 10^{10}$ kg m$^{-3}$, the reference temperature $T_0 = 10^4$ K, and the typical length scale of the problem $L_0 = 1$ Mm. In the actual calculation, all variables are normalized by these three characteristic quantities and their combinations. Accordingly, the velocity, timescale, magnetic field, plasma pressure, current density, and resistivity are all normalized by $V_0 = \sqrt{RT_0}$, $\tau_0 = L_0/V_0$, $B_0 = \sqrt{\mu\rho_0 V_0^2}$, $P_0 = B_0^2/\mu$, $J_0 = B_0/(\mu L_0)$, and $\eta_0 = \mu L_0 V_0$, respectively. Here, $R$ is the gas constant and $\mu$ is the magnetic permeability of free space.

The computational domain spans $-12$ Mm $\leqslant x \leqslant 0$ Mm in the horizontal dimension and 0 Mm $\leqslant y \leqslant 15$ Mm in the vertical dimension. The top of the chromosphere is at $y = 0$ Mm. The center of the magnetic funnel is set at $x = 0$ Mm, so that the simulation region is symmetric around $x = 0$ Mm. The domain is covered by a nonuniform grid, both in the $x$ and $y$ dimensions. The grid spacing is $\delta x = \delta y = 25$ km for 0 Mm $\leqslant y \leqslant 4$ Mm, $\delta x = \delta y = 50$ km for 4 Mm $\leqslant y \leqslant 6$ Mm, and $\delta x = \delta y = 100$ km for $y \leqslant 6$ Mm. The simulation results tested with higher resolution are found to converge.

To solve the MHD equations, we employ a 2.5D resistive MHD scheme (Feng et al. 2011; Zhang et al. 2011), which has been applied before to study the magnetic-cloud-driven reconnection under real solar wind conditions, and also magnetic reconnection under solar coronal conditions. The numerical scheme of the model splits the resistive MHD equations into a fluid part and magnetic-induction part, whereby the fluid part is solved by the second-order Godunov-type central scheme and the magnetic part by the constrained transport approach (Ziegler 2004). For the time integration, the explicit second-order total variation diminishing Runge–Kutta time stepping is applied. This kind of splitting-based finite-volume scheme for ideal MHD equations has been validated to be remarkably stable even at very fine mesh resolutions, and thus it can handle the divergence constraint efficiently with low divergence error. With this model, the evolution process of magnetic reconnection in a long-thin Harris-type current sheet was, under the solar coronal conditions, investigated with different magnetic Reynolds numbers as high as $10^6$ (Feng et al. 2011; Zhang et al. 2011).

### 2.3. Initial and Boundary Conditions

Initially, the gas is in hydrostatic equilibrium and the temperature is prescribed by a hyperbolic tangent function,

$$T(y) = T_{\rm chr} + \frac{1}{2}(T_{\rm cor} - T_{\rm chr})\left[\tanh\left(\frac{y - y_{\rm cor}}{w_{\rm tr}}\right) + 1\right], \quad (12)$$

where $T_{\rm cor}$ and $T_{\rm chr}$ are the respective temperatures in the corona and chromosphere. We set $T_{\rm cor} = 1 \times 10^6$ K, $T_{\rm chr} = 2 \times 10^4$ K,

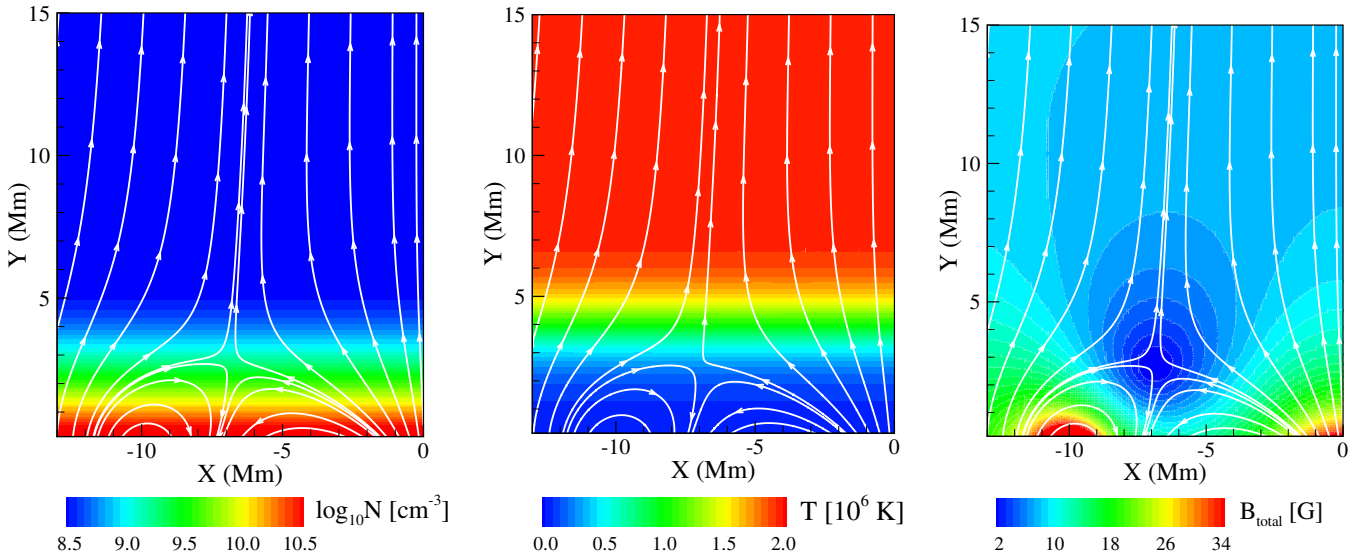


**Figure 2.** The initial distributions of number density, temperature, magnetic field strength, and magnetic field lines (white lines with arrows). That is, the distributions is at $t = 0$ minutes.

(A color version of this figure is available in the online journal.)

and $w_{\rm tr} = 1.5$ Mm. On the basis of the given function of temperature $T(y)$, the distributions of the pressure $p(y)$ and density $\rho(y)$ are derived by solving analytically the 1D hydrostatic equation,

$$\frac{dp(y)}{dy} = -\rho(y)g, \tag{13}$$

with the pressure given through the ideal gas equation,

$$p = \rho RT, \tag{14}$$

where $R$ is gas constant. The initial velocity is set equal to zero.

To get the magnetic configuration including the magnetically open funnel, the closed loops, and the null point, we compose the initial magnetic field using a superposition of two potential fields, which again is a potential field. One potential field describes the funnel structure as given by the analytical expression of Hackenberg et al. (2000). The other is generated by two infinite straight-line currents flowing along the line $x = -10$ Mm, $y = -0.7$ Mm and the line $x = 10$ Mm, $y = -0.7$ Mm. We simply add these two vector fields to generate the initial magnetic field. Figure 2 illustrates this constructed magnetic configuration and also the initial distributions of number density $N$, temperature $T$, and magnetic field strength $B_{\rm total}$.

After setting up the magnetic field configuration, we discern the loop region to be heated with Equation (11) based on following criteria: (1) both ends of the traced field lines should be located at the bottom boundary; (2) left end has a positive polarity. During the computation, we continuously heat the loop plasma to sustain the high temperature. Otherwise, the loops would cool down due to radiation loss. However, we will stop the heating once a closed field line reconnects with the funnel and thus becomes magnetically open.

The boundary conditions are defined as follows. At the right boundary, $x = 0$ Mm, all quantities are symmetric, as mentioned before. At the left side, $x = -12$ Mm, we employ open boundary conditions, i.e., we set the normal gradients of $\rho$, $\mathbf{u}$, $T$ to zero there and extrapolate $\mathbf{B}$ linearly. To ensure that upward propagating waves leave the computational domain without generating spurious reflections at the upper boundary ($y = 15$ Mm), we implemented free boundary conditions at the top, with virtual mesh points added in the same way as done by Yokoyama & Shibata (1996). At the lower boundary ($y = 0$ Mm), the density $\rho$ and temperature $T$ are fixed. We prescribe the horizontal component of the velocity as $v_x(y = 0) = 3(1. - \exp(-|0.5x|))$ km s$^{-1}$ to mimic the supergranular plasma convection. At the center of the funnel the plasma is at rest, $v_x = 0$ km s$^{-1}$, and in the cell interior it is driven with up to $v_x \approx 3$ km s$^{-1}$ toward the funnel. Here we use a rather large value for the supergranular motion, simply to speed up the magnetic reconnection between the funnel and the hot dense loop. From observations, the typical horizontal velocity of supergranular advection in the chromospheric network is found to be 1.0–1.5 km s$^{-1}$ based on the local correlation tracking method (Yi & Molowny-Horas 1995). The advection speed ($\sim$3 km s$^{-1}$) chosen here is close to the averaged observational value, but a little bit larger just for more clear illustration. The simulation result with the advection speed of 3 km s$^{-1}$ is shown to be similar to that with 1 km s$^{-1}$. At the bottom we set the vertical component of the velocity $v_y$ to zero, unless it is negative at the neighboring points in the computational domain. In that case, $v_y$ is determined by linear extrapolation to allow plasma to be subducted. We initialize the values of the horizontal components $(B_x, B_z)$ of the magnetic field by assuming the second normal derivative to vanish. Then the divergence-free condition $\nabla \cdot \mathbf{B} = 0$ is used to determine the vertical component $(B_y)$ of the magnetic field.

## 3. NUMERICAL RESULTS

### 3.1. State before and after the Onset of Reconnection

Before the horizontal flow is initiated to drive the reconnection between the loop and the funnel, the system including radiative losses, heat conduction, and heating, is relaxed into a quasi-steady state after approximately 20 minutes of physical time. The top row of Figure 3 shows a snapshot of these quasi-steady solutions for the number density $N$, temperature $T$, thermal pressure $P$, and magnetic field in the form of

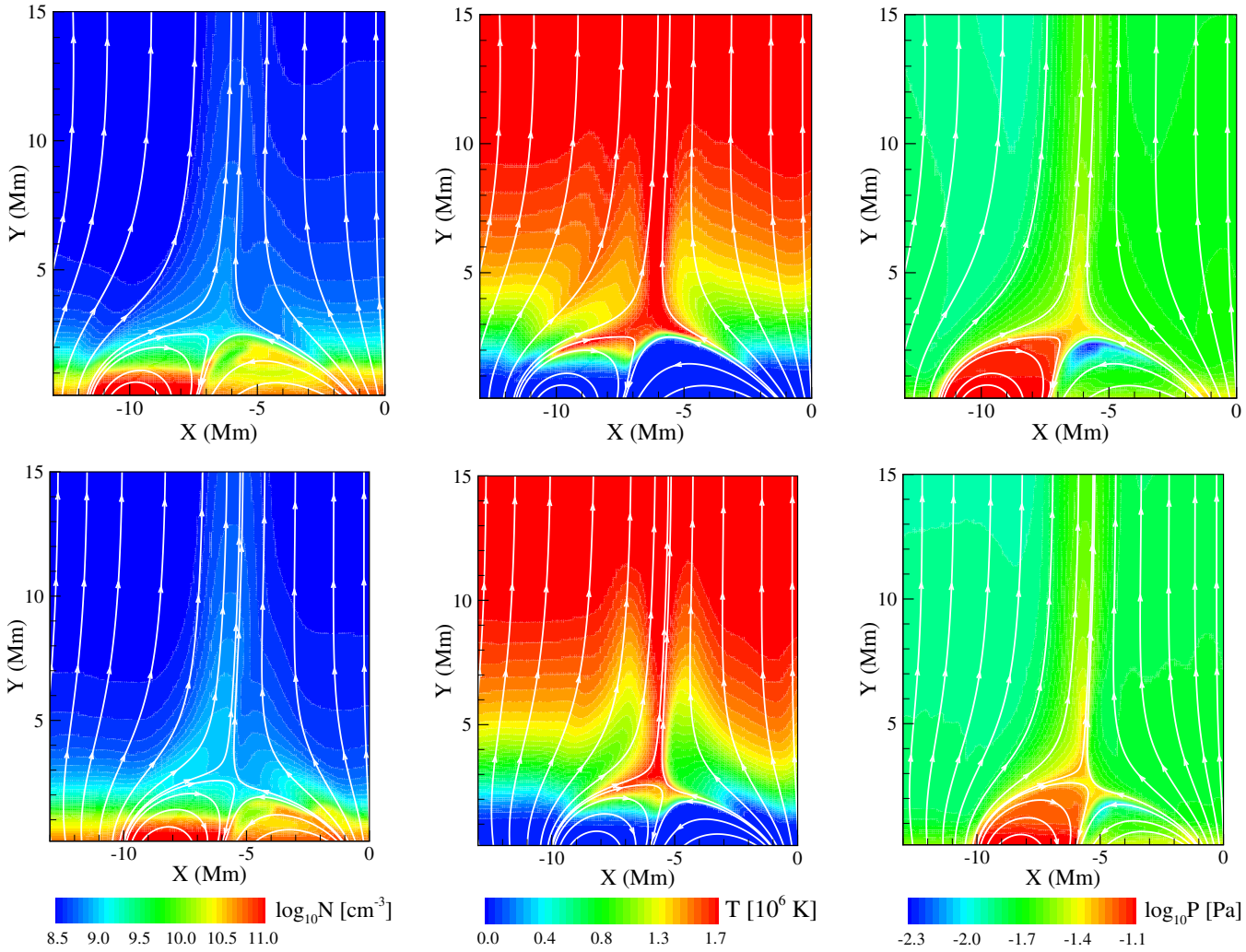


**Figure 3.** Distributions of number density $N$, temperature $T$, and thermal pressure $P$ at $t = 20$ minutes before the onset of reconnection (top row), and at $t = 23$ minutes after the onset of reconnection (bottom row). Streamlines denote the magnetic field lines.

(A color version of this figure is available in the online journal.)

streamlines. A snapshot after the reconnection between the loop and the funnel set following the horizontal driving is shown in the bottom row.

The bottom row of Figure 3 shows that the left loops have high density, high temperature, and high pressure as a result of more heat being deposited into this region. The typical values of the simulated number density and temperature of the outside loops are about $2.2 \times 10^{11}$ cm$^{-3}$ and $2.1 \times 10^4$ K in the upper chromosphere, and about $1.6 \times 10^9$ cm$^{-3}$ and $1.2 \times 10^6$ K near the top of the transition region, which are in agreement with the simulation results shown by Li & Habbal (2003). The magnetic field is deformed to deviate from the initial potential field distribution as shown in Figure 2. The loop to the right with the opposite magnetic direction (between hot loop and funnel) has high density, low temperature, and low pressure, due to large radiative losses and the lack of extra heating. The open funnel is evolving toward a quasi-stationary configuration that extends from a cool dense chromosphere to a hot tenuous corona with a transition region at a height of about 2.2 Mm.

After the horizontal flow driving the reconnection is initiated, as shown in the bottom row of Figure 3, the hot dense loop is carried toward the open funnel. Due to the stress produced by the driver, the interface between the hot dense loops and the ambient coronal field is deformed and a current sheet is generated around the magnetic null point. When the current density gets high enough, the reconnection between the field in the closed loop and the open funnel sets in. As a result, the material in the hot dense loop is released partly into the newly opened funnel field lines and partly into the newly reconnected closed loop. At the same time, the top of the cool loop at the right hand side is heated up by the released magnetic energy, although the radiative losses get larger there.

Figure 4 shows the resulting distributions of the current density $J$, the current-carrier velocity $u_d$, the temperature $T$, and the total speed $V_t$ at $t = 25.5$ minutes, which are zoomed-in around the area of reconnection. In the map of $u_d$, blue denotes those regions where the anomalous resistivity is switched off. We can see that an X-type reconnection takes place. In the resistivity region, the current density $J$ is extremely large, so that once the current-carrier velocity $u_d$ exceeds the limit $u_c$, the anomalous resistivity as determined by Equation (6) sets in. The temperature is enhanced in the resistivity region as a result of Joule dissipation. This enhancement is not restricted to the resistivity region but also present outside that region. Because of the large radiative losses at lower heights, the temperature enhancement is not as obvious in the lower atmosphere as

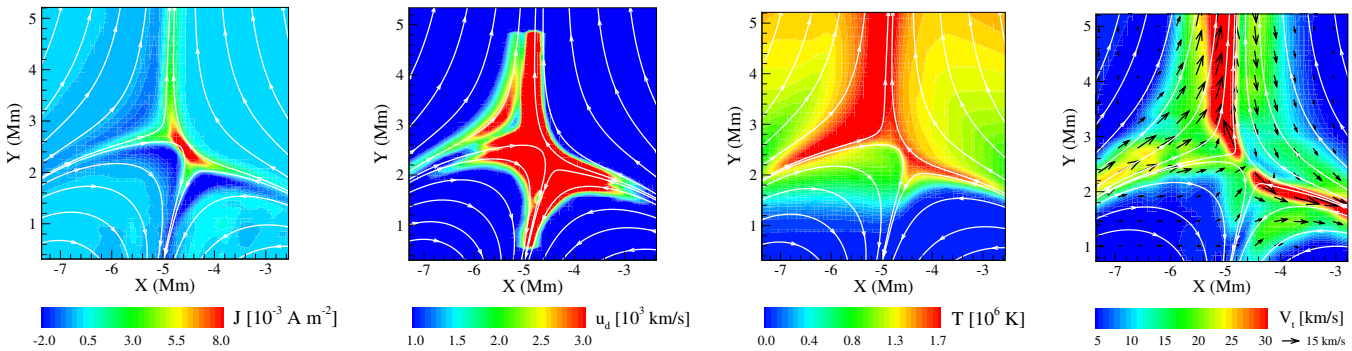


**Figure 4.** Distributions of current density $J$, current-carrier velocity $u_d$, temperature $T$, and total speed $V_t$ at $t = 25.5$ minutes. Zoom of the area around the reconnection region. Streamlines show the magnetic field lines, and black arrows denote the velocity. The length of the arrows are proportional to the speed of the plasma. As a reference the little arrow next to the right panel corresponds to 15 km s$^{-1}$. In the map of $u_d$, blue denotes the regions where the anomalous resistivity is switched off.

(A color version of this figure is available in the online journal.)

it is higher up. The magnetic tension force accelerates the heated plasma along with the frozen-in reconnected field lines, and ejects these from the resistivity region, both upward and downward as shown in the distribution of the velocity. The maximum velocities of the upward and downward motions are about 32 km s$^{-1}$ and 28 km s$^{-1}$, respectively. This speed of the outflow is comparable to the local Alfvén speed of $V_A = 30$ km s$^{-1}$ (at the height of 2.5 Mm, i.e., near the transition region). It should be mentioned that in the simulation, the local Alfvén velocity outside the reconnection site is time varying. As the reconnection site gradually moves from the corona to the bottom of the transition region (see Figure 6 for a demonstration), the local Alfvén velocity changes from hundreds of km s$^{-1}$ to tens of km s$^{-1}$.

### 3.2. Tracing Mass Motions through the Reconnection Site

To trace the motions of the plasma originally contained in the hot loop, we solve an additional passive equation simultaneously together with the MHD equations (Odstrčil & Pizzo 1999),

$$\frac{\partial \rho_c}{\partial t} + \nabla \cdot \rho_c \mathbf{u} = 0, \quad (15)$$

where $\rho_c$ is the density of the traced particles. Initially we define the traced-particle density $\rho_c$ so that it is constant in the closed loop and zero outside (see Figure 5, bottom left). The passive continuity equation then ensures that $\rho_c$ is advected in the background flow. Just as test particles would do, $\rho_c$ then shows where the plasma in the originally closed loop will move to. Figure 5 shows the evolution of vertical velocity $V_y$ (the top row) and the density $\rho_c$ tracing the plasma (the bottom row) at different times before and after the onset of reconnection ($t = 20$, 23, and 28 minutes).

From Figure 5, we can see that before the onset of reconnection, the velocity along the open funnel is almost zero, and the traced-particle-density $\rho_c$ is still restricted within the closed loop. At $t = 23$ minutes when the horizontal flow has been switched on for 3 minutes, the traced hot loop starts to reconnect with the open funnel, thus producing both upward and downward outflows. This also results in new open fields and small secondary loops. Accelerated by the tension force as well as the gradient force of thermal pressure, the plasma on the newly opened field lines flows continuously upward. The downward flow forces the small loop to submerge below the photosphere. Also, there is evidence for an upward flow along the reconnected loops, which is the result of the post-reconnection pressure gradient (Del Zanna et al. 2011; Bradshaw et al. 2011) as shown in Figure 6. This is not a result of the evaporation associated with the strong heat conduction back from the corona (Miyagoshi & Yokoyama 2004).

During the reconnection phase, the plasma that was originally part of the hot dense loop is carried outward by the flow. Furthermore, plasma is flowing downward along the open funnel near the reconnection region, and thereby pushes material into the diffusion region. At $t = 23$ minutes the traced-particle density $\rho_c$ is released from the closed tube. Material partly flows downward and partly flows upward, with some of it not passing through the reconnection site (see Figure 5). At $t = 28$ minutes, the location of the reconnection region migrates downward. The upward-moving part of the traced particles reaches high altitudes, up to about 12 Mm. The downward-moving part of the traced particles fills the secondary loops below (see Figure 5, bottom right). However, the traced particles from the formerly closed hot loop do not reach 15 Mm, owing to insufficient energy for accelerating the upward flow.

To the left of the upward flow, there are significant downflows along open fields, which occur due to the lack of the heating and acceleration that is required for the upward flow to become real solar wind outflow. Therefore, eventually the material falls down again as enforced by solar gravity. To lift the plasma out into the solar wind, extended heating would indeed be required, which is not included in this model that only considers the mass input at the coronal base. Nevertheless, it is obvious that the process of reconnection described here basically confirms the new scenario of solar wind origin as proposed by Tu et al. (2005a, 2005b).

To investigate the driving forces, Figure 6 presents the distributions of the perpendicular and field-aligned components of the Lorentz force $F_L$, the gas pressure force $(F_p)_\perp$ and $(F_p)_\parallel$, the gravitational force $g_\parallel$, and the total force $(F_t)_\perp$ and $(F_t)_\parallel$ per unit mass at $t = 25.5$ minutes. In the top row, the black arrows indicate the direction of the perpendicular component of the forces, and colors show the values of the perpendicular component of the forces. In the bottom row, the colors display the field-aligned components of the forces with positive (negative) values corresponding to the upward (downward) direction. In the last column, the red lines show the isocontour of $(F_t)_\perp$ at 3200 m s$^{-2}$.

From this figure, we can see that around the reconnection region, the Lorentz force $F_L$ is dominant, although the

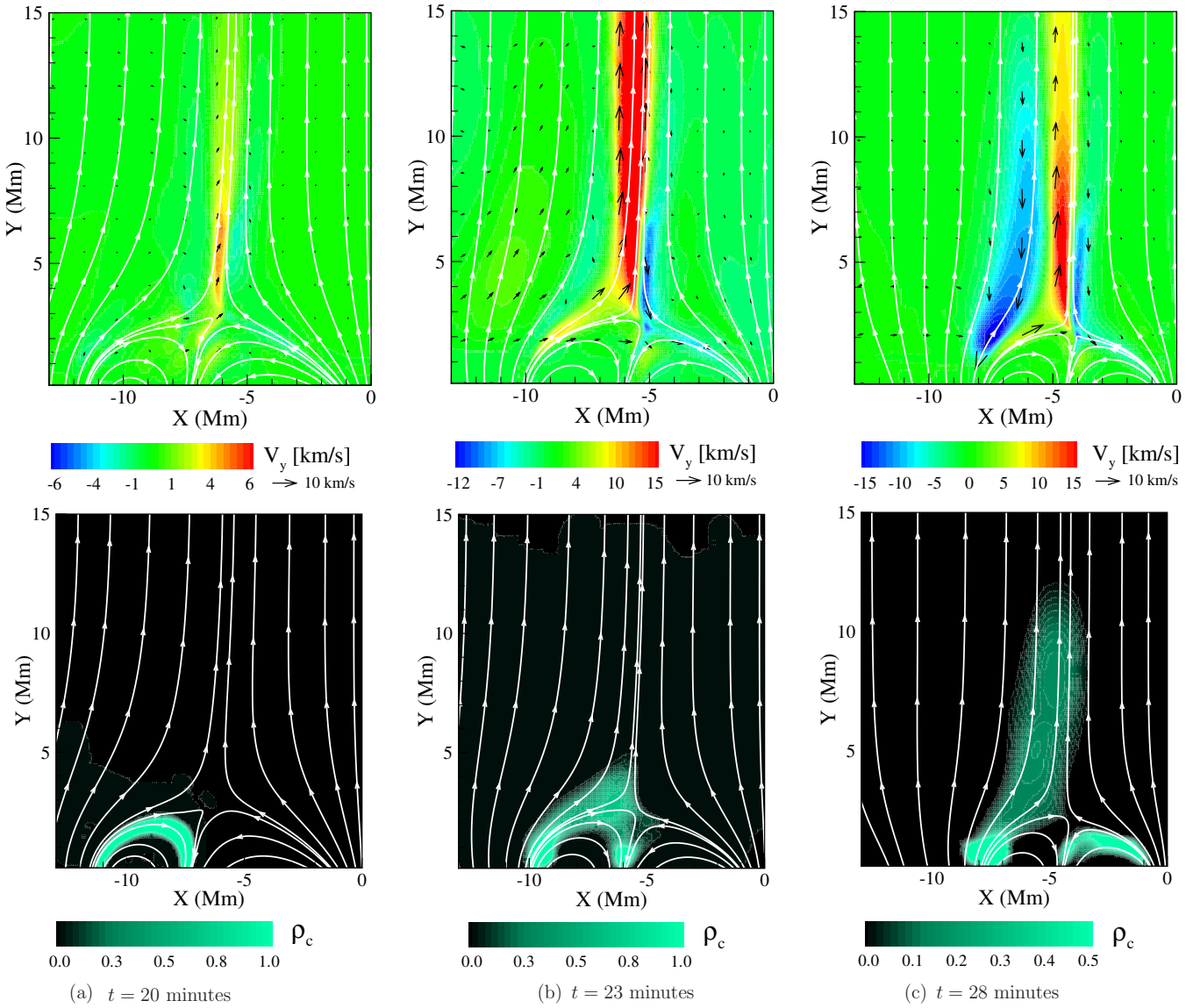


**Figure 5.** Calculated distributions of vertical velocity $V_y$ (top row) and density $\rho_c$ tracing the plasma (bottom row) at $t = 20$ minutes before the onset of reconnection (left column), $t = 23$ minutes (middle column), and $t = 28$ minutes (right column) after the onset of reconnection. In the top row black arrows denote the velocity, and in the bottom row streamlines indicate the magnetic field lines.

(A color version of this figure is available in the online journal.)

perpendicular component of the gradient of the gas pressure $(F_p)_\perp$ is large. In the inflow region, $F_L$ pushes the plasma, together with the frozen-in reconnected field lines, into the resistivity region. However, in the outflow region, $F_L$ pulls out the hot plasma along with the frozen-in magnetic field from the resistivity region. Around the reconnection region, the field-aligned component $(F_p)_\parallel$ of the gas pressure gradient is much larger than the field-aligned gravity $g_\parallel$. Near the reconnection region, the large value of $(F_p)_\parallel$ drives the reconnection flow upward and downward along the magnetic fields. Obviously, there exists upward $-\nabla P$ along the opened field lines, which drives the plasma from the hot loop to flow outward. However, due to the gas pressure enhancement in the outflow region as shown in Figure 3, there is a very small region near the left-hand outflow region where $(F_p)_\parallel$ becomes negative, so that the upward flowing plasma along the high-pressure leg of the closed loop gets decelerated there. Away from this region, the large positive $(F_p)_\parallel$ makes the plasma stream outward again along the reconnected field lines.

Therefore, there are two components of upward plasma: one originates from the plasma moving through the reconnection region, and the other is from the high-pressure leg of the newly-opened loops. Evidently, the first component of the upward moving plasma is smaller than the second component, which is due to the fact that only a small part of the plasma of the formerly closed hot loop can go through the reconnection region.

### *3.3. Mass Loss to the Wind*

In Figure 7, we show the tube-aligned velocity and mass flow rate along the open flux tube, with the horizontal coordinate denoting the length along the tube. The mass flow rate is computed here as the multiplication product of number density, tube-aligned velocity, and cross-sectional area of the open flux tube. The cross-sectional area is the simulated width of the open flux tube (approximately 300 km in this simulation) times the assumed unit length in the third direction (1 cm). The properties at $t = 22.0$, 24.0, and 25.5 minutes are displayed. We keep

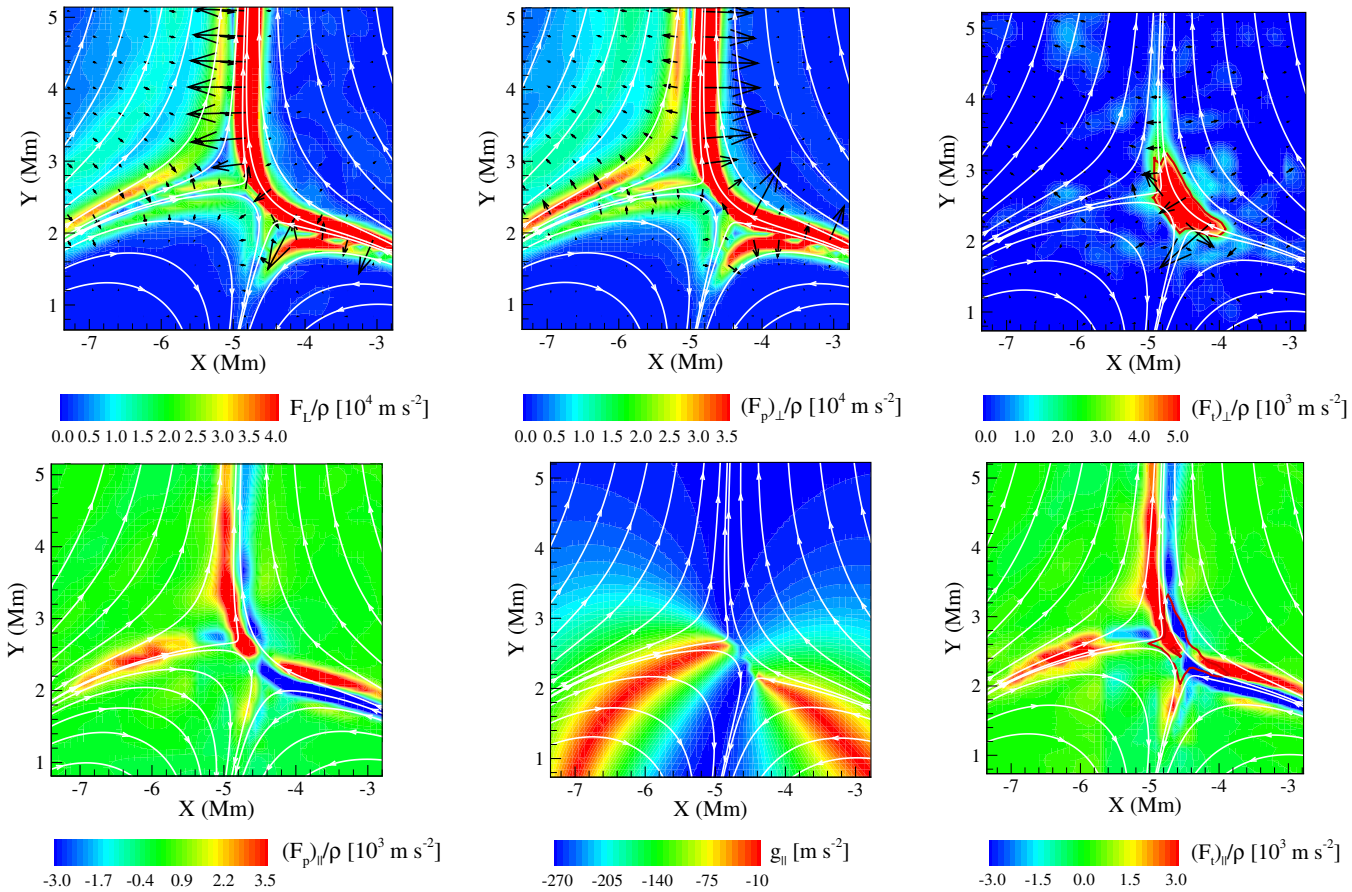


**Figure 6.** Calculated distributions of the perpendicular and field-aligned components of the Lorentz force $F_L$, the gas pressure force $(F_p)_\perp$ and $(F_p)_\parallel$, the gravity $g_\parallel$, and the total force $(F_t)_\perp$ and $(F_t)_\parallel$ per unit mass at $t = 25.5$ minutes, where streamlines show the magnetic field lines. In the top row, the black arrows denote the direction of the perpendicular component of the forces, and colors show the values of the perpendicular component of the forces. In the bottom row, colors display the values of the field-aligned component of the forces. Positive (negative) values correspond to the upward (downward) direction. In the last column, the red lines show the isocontour of $(F_t)_\perp$ at 3200 m s$^{-2}$.

(A color version of this figure is available in the online journal.)

track of the flux tube based on the following criteria: at first, the open flux tube is part of the open funnel region, i.e., to the right of the reconnection site. As time increases, it reconnects with the hot dense loop, and a new open flux tube forms with one endpoint connected to the originally chosen flux tube and the other to the hot dense loop. From this moment on, the open flux tube we choose is defined as this new open flux tube.

From Figure 7, it is clear that at $t = 22$ minutes the flow along the chosen flux tube is weak. At that time, the chosen flux tube still had not reconnected with the hot loop. After it reconnected with the hot dense loop, a new open flux tube developed with one endpoint from the hot loop and the other from the chosen open flux tube at $t = 22$ minutes. At $t = 24$ minutes, the variation of the tube-aligned velocity and mass flow rate along this new open flux tube are shown. The plasma streams upward along this new tube, and the speed is about 15 km s$^{-1}$ close to the top boundary of the computational domain. More importantly, the outward directed mass flow rate in this newly formed flux tube is approximately constant, and the value is about $5 \times 10^{22}$ s$^{-1}$.

The mass flow rate we find at the base of the outflow corresponds to a particle flux of about $10^{15}$ s$^{-1}$ cm$^{-2}$. Accounting for the radial expansion from the Sun to 1 AU (factor $215^2$), i.e., a factor of 30 associated with the expansion of the funnel, and finally another factor of 5 associated with the large-scale non-radial expansion of the wind (Kopp & Holzer 1976; Suzuki & Inutsuka 2005), we end up with $1.5 \times 10^8$ s$^{-1}$ cm$^{-2}$. Actually, this mass flux density corresponds well to the *Ulysses* measurements of the solar wind mass flux density at 1 AU, which is about $2.0 \times 10^8$ s$^{-1}$ cm$^{-2}$ (Neugebauer 1999). Based on these results, we may conclude that a sufficient amount of material can be released from small closed loops through reconnection with neighboring open structures, and thus can feed the mass into the source region of the solar wind.

However, at $t = 25.5$ minutes when this new open flux tube is far away from the reconnection region, the upward flowing material along this tube cannot be accelerated any longer and drops back down. Correspondingly, the mass flow rate falls as well. Certainly, to drive the upflow all the way out to 1 AU, further extended heating and acceleration of the plasma has to occur. The process we described here just provides the required mass for the wind.

## 4. SUMMARY AND DISCUSSION

In this study, we use a 2.5D MHD model with a computational domain ranging from the upper chromosphere to the lower corona in order to examine the scenario suggested by Tu et al. (2005a, 2005b) for the origin of the solar wind. A realistic energy equation is considered, including heat conduction, radiative losses, and coronal heating. We prescribe the heat input in a closed magnetic field region, in order to produce a hot dense loop which has characteristics similar to the CBPs

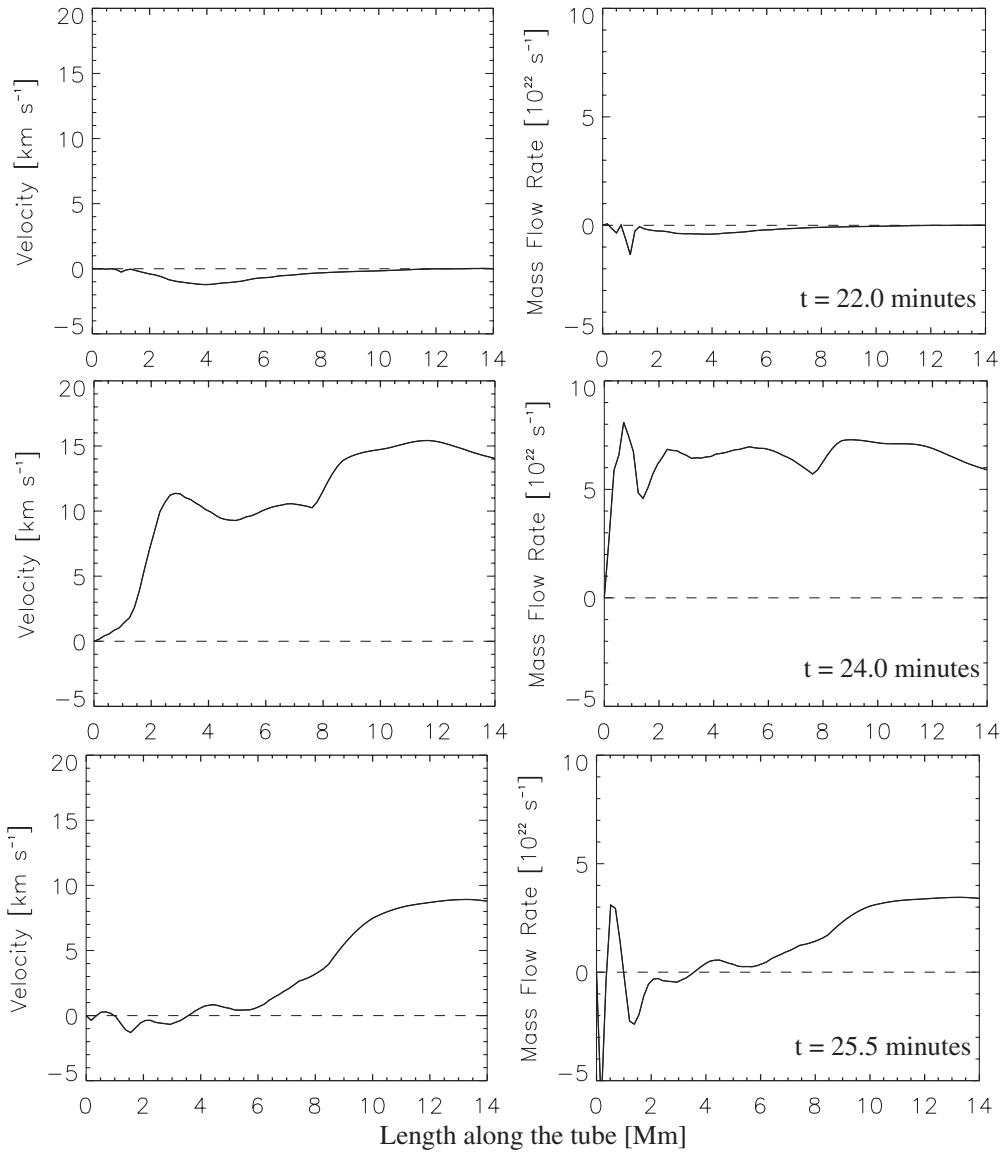


**Figure 7.** Calculated tube-aligned velocity and mass flow rate along the chosen tubes at $t = 22.0,\ 24.0$, and 25.5 minutes.

from solar observations. With the MHD model, we simulate the reconnection between a magnetically open coronal funnel and hot dense loops, which are horizontally advected by the supergranular flow toward the network lane.

The numerical results obtained support the scenario of solar wind origin proposed by Tu et al. (2005a, 2005b). Carried along by the supergranular convective motions in the photosphere, the closed loops move toward the edges of the supergranular network cells, where they reconnect with open funnel fields. The tension force of the magnetic field and the post-reconnection gradient force of the thermal pressure accelerate a transient upward-directed flow along the newly created open flux tube. This flow transports the plasma from the formerly hot dense loop into the nascent solar wind. The corresponding downward-directed reconnection flow forces secondary loops to be subducted back into the photosphere.

Analyzing the properties of the selected flux tubes, we find that the mass flow rate along the flux tube is basically consistent with that of the solar wind derived from in situ observations. This suggests that the plasma for the solar wind could be supplied from the closed loops next to the open funnels in the network lanes separating the super-granular cells. In our simulation results (e.g., in Figures 5 and 7), we do not see any prominent upflow from the footpoint of pre-existing open funnel. Therefore, the transient injection of plasma into the solar wind as found in our study is fundamentally different from the traditional concept of a continuous vertical flow through a tube rooted deeply in the photosphere. This latter concept was implicitly assumed in previous solar wind models including the chromosphere (e.g., Withbroe 1988; Hansteen & Leer 1995).

The reconnection event and its associated injection of mass into the upper atmosphere as we describe them here can also be related to the observed jets in coronal holes. While our reconnection scenario is different from the standard scenario suggested by Shibata et al. (1992), both scenarios share fundamental observable consequences. In particular, in a multipolar region our model can also produce a transient injection of plasma on open field lines. The difference is that in the standard cartoon scenario for the coronal hole jets (e.g., Moore et al. 2010) a closed region sits below an open region in a scaled-down streamer-like configuration. There, reconnection above the closed region then accelerates plasma that was already present in the open region.

In contrast, in our model the mass for the outburst comes from a closed region that is moving toward the open field region. Evidence for the imprint of the small X-ray jets has been recently found in the solar wind (Neugebauer 2012), and detailed observations of the coronal hole jets using imaging (e.g., Tian et al. 2011) and spectroscopic data (e.g., He et al. 2010a) exist. Further work using forward modeling including a spectral synthesis of the model data will have to show which of the proposed models might better fit the coronal-hole jet observations.

In this work we investigated only the injection of plasma at the very base of the solar wind. Clearly, some further heating and acceleration of the plasma is needed to power the solar wind outflow. Axford & McKenzie (1992) and Axford et al. (1999) assumed that small-scale reconnection between the closed loops and open fields takes place at the boundaries of the supergranulation network pattern, and thus produces high-frequency Alfvén waves. The damping of these waves could provide the required heating and acceleration for the solar wind, as it was shown by Marsch & Tu (1997) and Tu & Marsch (1997). Suzuki & Inutsuka (2005, 2006) suggested that footpoint motions in the photosphere will excite low-frequency Alfvén waves, whose conversion and dissipation are an effective mechanism for heating and acceleration of the solar wind, too. In the future, we will study the effect of such processes on the heating and acceleration of the outflow in the context of the present scenario. Also, the Alfvén waves produced by reconnection need to be investigated to explore their interaction with the upward movement of plasma.

Furthermore, this MHD model needs to be extended to a fully three-dimensional simulation, in which physically and numerically sound boundary conditions are introduced, and which will self-consistently enforce magnetic reconnection between open funnels and closed loops in more realistic solar environment. It should be pointed out that the current work is limited to the process of a single loop reconnecting with a funnel, without considering the recurrent reconnection of multiple loops. Yet recurrent reconnection seems to be necessary for ensuring continuous and sufficient mass supply. In our future work, we will also incorporate such recurrent reconnection in the model. Promisingly, new observational diagnostics of the solar wind source regions made with high spatial and temporal resolution by the *Solar Dynamics Observatory* and the upcoming IRIS UV and EUV spectrograph may help to further constrain and develop the model proposed here.

L.P. thanks Z.-W. Ma, H. Tian, Q.-M. Lu and S.-H. Zhang for helpful discussions. This work at Peking University is supported by NSFC under contract Nos. 40931055, 41174148, 41231069, and 41222032. L.P. is also supported by NSFC under contract Nos. 41031066, and 41204127, as well as China Postdoctoral Science Foundation under contract No. 452101480342. H.P. gratefully acknowledges the kind hospitality at Peking University. The numerical calculation has been completed on SIGMA Cluster computing system of the State Key Laboratory for Space Weather.

## REFERENCES

Abbett, W. P. 2007, ApJ, 665, 1469
Aiouaz, T., Peter, H., & Keppens, R. 2005, A&A, 442, L35
Axford, W. I., & McKenzie, J. F. 1992, in Proc. COSPAR Colloq., Solar Wind Seven Colloquium, ed. E. Marsch & R. Schwenn (Oxford: Pergamon Press), 1
Axford, W. I., McKenzie, J. F., Sukhorukova, G. V., et al. 1999, SSRv, 87, 25
Beatty, J. K. 2007, S&T, 113, 060000
Biermann, L. 1951, ZA, 29, 274
Bingert, S., & Peter, H. 2011, A&A, 530, A112
Bradshaw, S. J., Aulanier, G., & Del Zanna, G. 2011, ApJ, 743, 66
Büchner, J., & Elkina, N. 2005, SSRv, 121, 237
Büchner, J., & Nikutowski, B. 2005, in Solar Wind 11/SOHO 16, Connecting Sun and Heliosphere, ed. B. Fleck, T. H. Zurbuchen, & H. Lacoste (ESA SP-592; Noordwijk: ESA), 141
Büchner, J., Nikutowski, B., & Otto, A. 2004, in SOHO 15 Coronal Heating, ed. R. W. Walsh, J. Ireland, D. Danesy, & B. Fleck (ESA SP-575; Noordwijk: ESA), 23
Chen, Y., & Hu, Y. Q. 2001, SoPh, 199, 371
Cirtain, J. W., Golub, L., Lundquist, L., et al. 2007, Sci, 318, 1580
Cook, J. W., Cheng, C.-C., Jacobs, V. L., & Antiochos, S. K. 1989, ApJ, 338, 1176
Cranmer, S. R., van Ballegooijen, A. A., & Edgar, R. J. 2007, ApJS, 171, 520
Del Zanna, G., Aulanier, G., Klein, K.-L., & Török, T. 2011, A&A, 526, A137
Dere, K. P. 2008, A&A, 491, 561
Doschek, G. A., Landi, E., Warren, H. P., & Harra, L. K. 2010, ApJ, 710, 1806
Feldman, U., Landi, E., & Schwadron, N. A. 2005, JGR, 110, 7109
Feng, X., Yang, L., Xiang, C., et al. 2012, SoPh, 69
Feng, X., Zhang, S., Xiang, C., et al. 2011, ApJ, 734, 50
Forbes, T. G., & Malherbe, J. M. 1991, SoPh, 135, 361
Gudiksen, B. V., & Nordlund, Å. 2002, ApJL, 572, L113
Gudiksen, B. V., & Nordlund, Å. 2005, ApJ, 618, 1020
Hackenberg, P., Marsch, E., & Mann, G. 2000, A&A, 360, 1139
Hammer, R. 1982a, ApJ, 259, 779
Hammer, R. 1982b, ApJ, 259, 767
Hansteen, V. H., & Leer, E. 1995, JGR, 100, 21577
Hassler, D. M., Dammasch, I. E., Lemaire, P., et al. 1999, Sci, 283, 810
He, J.-S., Marsch, E., Curdt, W., et al. 2010a, A&A, 519, A49
He, J.-S., Marsch, E., Tu, C.-Y., Guo, L.-J., & Tian, H. 2010b, A&A, 516, A14
He, J.-S., Tu, C.-Y., & Marsch, E. 2007, A&A, 468, 307
He, J.-S., Tu, C.-Y., & Marsch, E. 2008, SoPh, 250, 147
He, J.-S., Tu, C.-Y., Tian, H., & Marsch, E. 2010c, AdSpR, 45, 303
Hollweg, J. V. 1986, JGR, 91, 4111
Hollweg, J. V., & Isenberg, P. A. 2002, JGR, 107, 1147
Kamio, S., Hara, H., Watanabe, T., et al. 2007, PASJ, 59, 757
Kopp, R. A., & Holzer, T. E. 1976, SoPh, 49, 43
Leer, E., & Holzer, T. E. 1980, JGR, 85, 4681
Li, B., Li, X., Hu, Y.-Q., & Habbal, S. R. 2004, JGR, 109, 7103
Li, X., & Habbal, S. R. 2003, ApJL, 598, L125
Marsch, E. 2006, in IAU Symp. 233, Solar Activity and its Magnetic Origin, ed. V. Bothmer & A. A. Hady (Cambridge: Cambridge Univ. Press), 259
Marsch, E., & Tu, C.-Y. 1997, SoPh, 176, 87
Matsumoto, T., & Suzuki, T. K. 2012, ApJ, 749, 8
Miyagoshi, T., & Yokoyama, T. 2004, ApJ, 614, 1042
Moore, R. L., Cirtain, J. W., Sterling, A. C., & Falconer, D. A. 2010, ApJ, 720, 757
Neugebauer, M. 1999, RvGeo, 37, 107
Neugebauer, M. 2012, ApJ, 750, 50
Nishizuka, N., Shimizu, M., Nakamura, T., et al. 2008, ApJL, 683, L83
Odstrčil, D., & Pizzo, V. J. 1999, JGR, 104, 483
Parker, E. N. 1958, ApJ, 128, 664
Parker, E. N. 1972, ApJ, 174, 499
Peter, H., Gudiksen, B. V., & Nordlund, Å. 2004, ApJL, 617, L85
Peter, H., Gudiksen, B. V., & Nordlund, Å. 2006, ApJ, 638, 1086
Peter, H., & Judge, P. G. 1999, ApJ, 522, 1148
Riley, P., Linker, J. A., & Mikić, Z. 2001, JGR, 106, 15889
Santos, J. C., & Büchner, J. 2007, ASTRA, 3, 29
Shibata, K., Ishido, Y., Acton, L. W., et al. 1992, PASJ, 44, L173
Shimojo, M., Shibata, K., Yokoyama, T., & Hori, K. 2001, ApJ, 550, 1051
Suzuki, T. K., & Inutsuka, S.-i. 2005, ApJL, 632, L49
Suzuki, T. K., & Inutsuka, S.-i. 2006, JGR, 111, 6101
Tian, H., McIntosh, S. W., Rifal Habbal, S., & He, J. 2011, ApJ, 736, 130
Tian, H., Tu, C., Marsch, E., He, J., & Kamio, S. 2010, ApJL, 709, L88
Tian, H., Tu, C.-Y., Marsch, E., He, J.-S., & Zhou, G.-Q. 2008, A&A, 478, 915
Treumann, R.-A. 2001, EP&S, 53, 453
Tu, C.-Y. 1988, JGR, 93, 7
Tu, C.-Y., & Marsch, E. 1997, SoPh, 171, 363
Tu, C.-Y., Zhou, C., Marsch, E., et al. 2005a, in Solar Wind 11/SOHO 16, Connecting Sun and Heliosphere, ed. B. Fleck, T. H. Zurbuchen, & H. Lacoste (ESA SP-592; Noordwijk: ESA), 131
Tu, C.-Y., Zhou, C., Marsch, E., et al. 2005b, Sci, 308, 519
van Ballegooijen, A. A. 1986, ApJ, 311, 1001

van der Holst, B., Manchester, W. B., Frazin, R. A., et al. 2010, ApJ, 725, 1373
Verdini, A., Velli, M., Matthaeus, W. H., Oughton, S., & Dmitruk, P. 2010, ApJL, 708, L116
Vernazza, J. E., Avrett, E. H., & Loeser, R. 1981, ApJS, 45, 635
Wang, Y.-M., & Sheeley, N. R., Jr. 1991, ApJL, 372, L45
Whang, Y. C., & Chang, C. C. 1965, JGR, 70, 4175
Withbroe, G. L. 1988, ApJ, 325, 442
Xia, L. D., Marsch, E., & Wilhelm, K. 2004, A&A, 424, 1025
Yang, L., Feng, X., Xiang, C., Zhang, S., & Wu, S. T. 2011, SoPh, 271, 91
Yi, Z., & Molowny-Horas, R. 1995, A&A, 295, 199
Yokoyama, T., & Shibata, K. 1994, ApJL, 436, L197
Yokoyama, T., & Shibata, K. 1995, Natur, 375, 42
Yokoyama, T., & Shibata, K. 1996, PASJ, 48, 353
Zhang, S.-H., Feng, X.-S., Wang, Y., & Yang, L.-P. 2011, ChPhL, 28, 089601
Zhang, T. X., & Wu, S. T. 2009, JGR, 114, 5107
Ziegler, U. 2004, JCoPh, 196, 393